Available online at www.sciencedirect.com
SCIENCE DIRECT
Earth and Planetary Science Letters 245 (2006) 278–288
EPSL
www.elsevier.com/locate/epsl

Bubble nucleation as a trigger for xenolith entrapment in mantle melts

Nadav G. Lensky [a,b,*], Ron W. Niebo [c], John R. Holloway [c], Vladimir Lyakhovsky [a], Oded Navon [b]

[a] Geological Survey of Israel, Jerusalem 95501, Israel
[b] Institute of Earth sciences, The Hebrew University of Jerusalem, Jerusalem 91904, Israel
[c] Department of Geological Sciences and Department of Chemistry and Biochemistry, Arizona State University, Tempe, AZ 85827, USA

Received 1 June 2005; received in revised form 24 November 2005; accepted 29 November 2005
Available online 5 April 2006
Editor: K. Farley

Abstract

Melts formed by small degrees of partial melting are rich in volatiles and may reach critical supersaturation during slow ascent or due to partial crystallization. Following nucleation, the bubbles grow and, if magma volume is confined, the surrounding walls deform and pressure increases. If pressurization is large enough and fast enough, the surrounding rock may fracture. We performed experiments on the nucleation of CO_2 bubbles in mafic alkaline melt saturated at 1.5 GPa and 1350 °C and found that supersaturation of 100–300 MPa is needed to initiate nucleation. Modeling bubble growth, and accounting for compressibility of melt and the surrounding host rocks, we found that in alkaline basalts about 30% of the critical supersaturation pressure stresses the walls. Kimberlites, with stronger dependence of solubility on pressure may recover about 45% of the supersaturation pressure. This is more than enough to cause brittle failure of the wall rocks, if pressurization is fast enough. The pressurization time scale is of the order of seconds to days, depending mostly on the diffusivity of CO_2 and on the bubble number density. This time scale is much shorter than the Maxwell relaxation time of the mantle rocks, or the characteristic time for flow back towards the source. Thus the host rocks are expected to respond elastically and fail in a brittle mode. Such event can form xenoliths and initiate dikes that allow the fast transport of the magma and its xenoliths to the surface. This mechanism may also explain the limited depth range spanned by most of the xenoliths sampled by individual eruptions in many localities.

Keywords: diamonds; xenolith; kimberlite; nucleation; bubbles

1. Introduction

Mantle-derived xenoliths and their host alkaline magmas show evidence that they originate at depths of tens and even hundreds of kilometers in the Earth's mantle (e.g., [1–5]). Limited reaction between xenoliths and the magma, and lack of thermal equilibration of xenoliths suggest short transport times. For example, dissolution experiments demonstrated that mantle-derived garnet crystals survive in kimberlitic melt for only several hours even at near solidus temperatures [6]. Similarly, Ar–Ar diffusion data in phlogopite grains in diamond-bearing xenoliths indicate transport time of hours to days [7]. These and

* Corresponding author. Geological Survey of Israel, Jerusalem 95501, Israel. Tel.: +972 2 5314 259; fax: +972 2 5380 688.
E-mail address: nadavl@gsi.gov.il (N.G. Lensky).

0012-821X/$ - see front matter © 2006 Elsevier B.V. All rights reserved.
doi:10.1016/j.epsl.2005.11.064

other data suggest that xenolith-bearing magmas ascend from the mantle at average rates of tens of m/s for kimberlites to tens of cm/s for alkaline basalts [8–10]. The fast ascent rates, as well as the transport of large xenoliths (up to tens of centimeters) indicate rapid magma ascent in dikes rather than in slow moving diapirs [8,11–13]. This raises the questions of how a dike is initiated and propagates, how do hot ductile rocks fracture under mantle pressures, and how is the mantle locally fragmented to form xenoliths.

Magma forms along grain boundaries, but its ascent rate at this stage is extremely slow. Even after it collects into channels or melt pockets, ascent remains slow as long as it depends on deformation of the matrix [14]. Nevertheless, formation of major cracks needed for high velocity flow in dikes and fast xenolith transport is not fully understood.

The high shear-strength of mantle rocks at the depth of xenolith collection precludes crack formation by any shear mechanism; the strength is estimated as 60–80% of the ambient pressure (i.e. a few GPa). The hot mantle rocks are too ductile to accumulate stresses over time, thus cracking is not expected under typical mantle strain rates. We propose that brittle failure may occur following a rapid loading.

Noting the general correlation between the presence of mantle xenoliths and the high volatile content of their host magmas, we examine the possible role of volatiles in trapping xenoliths. In many cases, xenoliths in a certain locality originate from a limited depth range, indicating a single trapping event. For example, many alkaline basalts carry only spinel peridotites while others may sample only lower crustal xenoliths; kimberlites bring mostly garnet peridotites but far fewer shallow mantle or lower crustal xenoliths. We suggest that such trapping is caused by discrete brittle failure events.

Based on our new experimental data on the nucleation of CO_2 bubbles in alkaline basaltic magma together with a bubble growth model, we suggest that fast growth of bubbles following nucleation may trigger the opening of cracks, initiate dikes in the otherwise ductile mantle and lead to trapping of xenoliths.

2. Nucleation experiments

Basic alkaline magmas can dissolve high proportions of volatiles, with CO_2 being an abundant species, and less soluble than H_2O. For example, moderately alkaline basalts dissolve more than 2 wt.% of CO_2 at 2 GPa, and solubility increases with alkalinity and pressure [15]. Basanitic lavas erupted underwater on the flanks of Hawaii record pre-eruption CO_2 contents of several wt.% [16]. Kimberlitic melts may dissolve ~30% CO_2 at pressures of 5 GPa [17].

During ascent, such volatile-rich magmas may reach saturation even at high pressure, and eventually, will reach the supersaturation levels needed for nucleation of bubbles. We present new data on the supersaturation needed for nucleating CO_2 bubbles in trachytic basalt at 1–1.5 GPa. These new data are used for exploring the role of volatiles in dike initiation and the trapping of xenolith by alkaline magmas.

2.1. Starting material

The starting material was a mixture of oxides and carbonates. Wustite and hematite were added to constrain the oxygen fugacity of the melt at NNO+2. CO_2 was introduced as Na_2CO_3 which results in 3.4 wt.% total CO_2, well in excess of the solubility at the pressures of the experiments [15]. This was confirmed by the presence of large, fluid-excess bubbles at the top of the capsule in the run product. The composition of the synthetic trachytic basalt starting material used in the experiments is (in wt.% recalculated to 100% on a volatile-free basis and with all iron as FeO): 54.04 SiO_2, 2.22 TiO_2, 12.69 Al_2O_3, 11.61 FeO, 7.25 MgO, 6.58 CaO, 4.85 Na_2O, and 0.76 K_2O (as determined by electron microprobe analysis of sample B-1-20, see Table 1 for experimental details). This composition differs slightly from that of a alkaline basalt, with higher SiO_2 and Na_2O, but lower Al_2O_3. However the measured CO_2 solubility and the calculated viscosity (and hence CO_2 diffusivity) of this composition are very close to that of a typical alkali basalt [15,18].

2.2. Experimental procedure

Approximately 20 mg of the CO_2-rich starting material was loaded in platinum capsules, packed in the pressure assembly and run in a 0.5 in. piston-cylinder at 1.5 GPa, 1350 °C for 4–5 h (see Pan et al. [19] for experimental details). CO_2 solubility at 1.5 GPa, 1350 °C was measured using SIMS and FTIR and is 1.4±0.2 wt.%, in good agreement with previous experimental data [15]. Dissolved H_2O was also present at levels of ~0.7 wt.%.

After saturation, pressure was lowered isothermally by slowly bleeding oil from the master cylinder. The response of the Pyrex–NaCl furnace assembly is very rapid, as evidenced by the shortest duration experiments. For example sample B-2-5 showed a high number density after 5 min at a final pressure of 1 GPa. The uncertainties in pressure precision are less

Table 1
Experimental conditions and results for decompression experiments

Sample name	Final pressure (GPa)	Time at final pressure (min)	Average bubble number density (bubbles/m^{-3})	Bubble size range diameter (μm)	Average bubble diameter (μm)	CO_2 concentration in glass [a] (wt.%)	H_2O concentration in glass [a] (wt.%)
B-6-20	1.3	20	$4.9\cdot10^{14}$	1–6	2	N/A	N/A
B-10-10	1.2	10	$2.5\cdot10^{15}$	0.8–1.2	1	1.31	1.05
B-5-20	1.2	20	$6.4\cdot10^{10}$	7–41	26	1.47	1.09
B-9-5	1.1	5	$3.4\cdot10^{14}$	1–8	2	N/A	N/A
B-6-5 [b]	1.0	5	$6.0\cdot10^{12}$	1–22	7	0.43	0.52
B-2-5	1.0	5	$3.8\cdot10^{10}$	6–31	20	1.44	0.82
B-1-8	1.0	8	$3.6\cdot10^{11}$	5–45	15	N/A	N/A
B-5-10	1.0	10	$2.4\cdot10^{11}$	5–28	12	1.55	0.83
B-1-20	1.0	20	$1.9\cdot10^{10}$	20–60	38	1.09	0.5
B-3-5	0.5	5	$3.7\cdot10^{12}$	2–46	18	0.66	0.8
B-2-10	0.5	10	$2.8\cdot10^{11}$	5–48	31	1.27	0.51
B-7-5	1.4	5				1.44	0.74
B-6-10	1.4	10				1.38	0.69
B-3-20	1.4	20				1.35	1.11
B-1-40	1.4	40				1.22	0.88
B-8-5	1.2	5				1.45	1.21
B-1-030	1.0	0.5				N/A	N/A
B-STD-1	1.5	240				1.16	0.63
B-STD-2	1.5	240				1.47	0.87
Pt-1 [c]	1.5	2					
Pt-2 [c]	1.5	3.5					
Pt-3 [c]	1.5	5					

N/A samples were not analyzed for volatile content.
[a] Volatile content measured by FTIR calibrated from SIMS data. Average 1σ is 0.13 for CO_2 and 0.14 for H_2O.
[b] B-6-5 was equilibrated for 5 h at 1300 °C, 1.5 GPa and then depressurized. All other samples with 'B' prefix were equilibrated for 4 h at 1350 °C, 1.5 GPa.
[c] Pt-1, Pt-2 and Pt-3 were run at 1350 °C and 1.5 GPa for the time given and then isobarically quenched.

than 3 MPa, and in accuracy less than 5 MPa using these furnace assemblies in this pressure range [20]. The CO_2 solubility data presented in Pan et al. [19] and Thibault and Holloway [21] suggest a precision in the range of 1 or 2 MPa in pressure measurement. Pressure was lowered at a decompression rate of ~10 MPa/s and held constant at a final pressure ranging between 1.4 and 0.5 GPa for 5–40 min. The experiments were then quenched at constant pressure at ~300 °C/s. Samples were liberated, sectioned, polished and examined microscopically for the presence of bubbles and crystals, and for the bubble number density, size distribution and volatile content. The C and H content of the glass in selected samples were determined by SIMS using a Cameca 3f at Arizona State University.

A record of the physical state of the samples as a function of run duration shows that at times less than 5 min at 1350 °C and 1.5 GPa, the experimental powder had melted and formed several large excess fluid-phase bubbles. Early excess fluid-phase bubbles can be seen in sample PT-1 (Fig. 1a). After 4 h, the melt has equilibrated and the remaining excess fluid has collected as a single bubble or a group of bubbles at the top of the capsule or adhering to capsule walls. The distinction between the pre-existing bubbles and the newly nucleated ones is clear (Fig. 1b).

2.3. Supersaturation

The experimental results are presented in Figs. 1–3 and Table 1. No nucleation was observed after decompressing the sample by 0.1 GPa (four runs held for 5–40 min at 1.4 GPa). Decompression yielded bubbles in a run held at 1.3 GPa for 20 min, and at 1.2 GPa for 10 and 20 min, but not after 5 min at 1.2 GPa. *We conclude that supersaturation of 0.1–0.3 GPa is the minimum needed for nucleation of CO_2 bubbles in alkaline basaltic melts*. This range of supersaturation is similar to that recorded for the nucleation of H_2O and H_2O–CO_2 bubbles in rhyolitic and dacitic melts [22–25].

The experiments were carried out above the liquidus temperature, and yielded no data on the possible role of heterogeneous nucleation. We observed heterogeneous distribution of bubbles (but no microlites) in only two samples, B-3-5 and B-6-5 that were

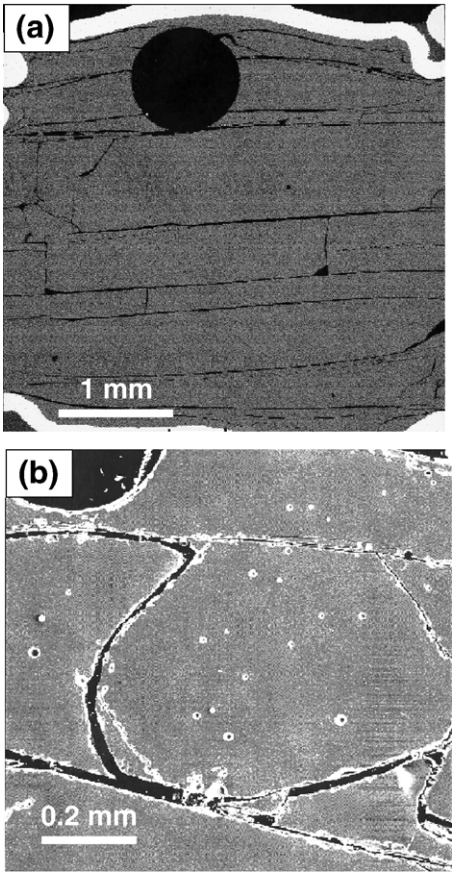

Fig. 1. Backscatter image of experimental charge before (a) and after (b) decompression. (a) Run B-STD-1. Note the formation of a large excess fluid-phase bubble located at the top of the capsule (black circle). Dark horizontal and vertical lines are cracks created during sample extraction. Bright areas are the walls of the platinum capsules. (b) Run B-5-10. The large black semi-circle at the upper left-hand corner is a large excess fluid-phase bubble. The small bubbles nucleated during decompression. Note the difference in the scale of the two figures.

decompressed by 1.0 and 0.5 GPa, respectively. The reason for that is not clear and, in any case, decompression in both runs was much higher than the critical supersaturation.

In Fig. 3, it can be seen that for a particular pressure drop the bubble number density generally decreases with increasing time at the lower pressure. This may reflect coalescence of bubbles. We also note the very high number density of bubbles, which in run B-10-10 reaches $2.5 \cdot 10^{15}$ bubbles/m^3.

3. Bubble nucleation and pressurization of ascending alkaline magmas

We examine two questions related to the pressurization following nucleation and bubble growth: (i) How much pressure can vesiculating magma impose on the elastic rocks surrounding it? (ii) How fast is the build-up of pressure?

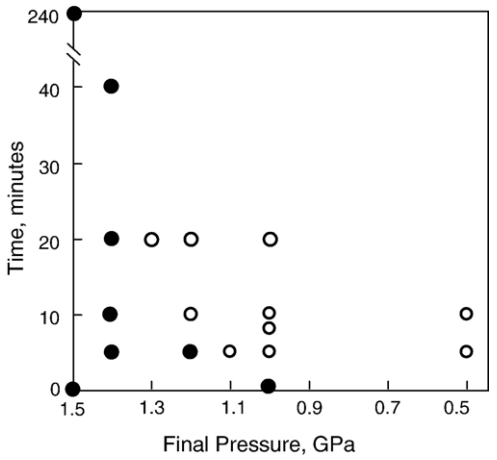

Fig. 2. Bubble nucleation experiments plotted as final pressure versus time for bubble nucleation. Initial pressure for all runs is 1.5 GPa. Closed circles represent runs that did not evolve bubbles and open circles represent runs that evolved bubbles. See Table 1 for experimental conditions and results.

In the following model, we consider a batch of magma that dissolves a certain concentration of volatiles (C_0) and ascends through an infinite medium. Temporal change of the pressure is schematically shown in Fig. 4. As the magma slowly decompresses, volatile solubility changes so that at some level (P_s) the magma becomes

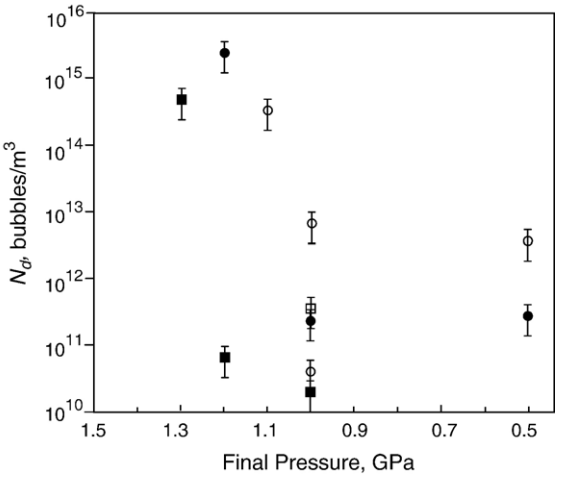

Fig. 3. Bubble number density in bubble-rich samples plotted against final pressure for different time intervals at the final pressure. Initial pressure for all runs is 1.5 GPa. Open circles 5 min, open squares 8 min, solid circles 10 min and solid squares 20 min runs. Error bars are ±50% relative due to the uncertainty associated with bubble counting. For any given final pressure, bubble number density is initially high and declines over time.

saturated and then supersaturation builds up. A certain degree of supersaturation, ΔP_n, is needed to nucleate bubbles in order to overcome the effect of surface tension. Hence, nucleation takes place at shallower level at a lower pressure, P_n. Alternatively, the magma may crystallize until it reaches saturation at pressure P_n and after an additional period of crystallization the needed supersaturation is reached [26].

At nucleation, the fluid in the nuclei is in chemical equilibrium with the surrounding melt and the fluid pressure in the bubble, P_b, is close to the sum of surface tension, $2\sigma/R$, and the solubility pressure, P_s (we use the term "fluid" because CO_2 in the bubbles at the relevant pressures is a supercritical fluid). If $P_b < P_s + 2\sigma/R$, the bubble shrinks and disappears. In the opposite case, the bubble expands, pressure in the bubble slightly decreases below P_s. The melt at the wall is now supersaturated and CO_2 is transferred into the bubble, leading to CO_2 diffusion from the melt towards the bubble-melt interface. At the initial stage, bubbles are small enough so that the diffusive flux of volatiles keeps the bubble pressure close to equilibrium with the supersaturated melt and growth is controlled by viscous deformation of the melt around the bubble (see Navon and Lyakhovsky [27] for detailed discussion). The duration of this stage is of the order of the viscous time scale, $\tau_{vis} = 4\eta/\Delta P_n \sim 10^{-6}$ s for the low viscosity (η) of the alkaline magmas and the large supersaturation (ΔP_n) (see Table 2). After a few microseconds, bubbles grew by more than order of magnitude, CO_2 diffusion is not efficient enough to keep high overpressure in the bubble, and it approaches the ambient pressure, P_a. At this stage the rate of growth is controlled by CO_2 diffusion from the melt shell surrounding the bubble, which keeps $P_b > P_a$ as long as the melt is supersaturated (dotted and heavy lines in Fig. 4). As the bubbly magma expands it deforms the surrounding rocks, which results in increase of ambient pressure. Bubble growth continues until ambient pressure reaches its final value, P_f, at which melt is saturated, diffusion ceases and bubble pressure is balanced by the ambient pressure and the surface tension. The quantitative description of these processes, presented in the following section, enables an estimate to be made of the maximum overpressure and the characteristic time of pressure buildup.

3.1. Buildup of pressure following nucleation

The maximum over-pressure, ΔP, is estimated based on mechanical and chemical equilibrium between the bubble and its surrounding melt shell. The magma is approximated as a close pack of spherical cells, each containing a bubble surrounded by a melt shell; at nucleation, the cell radius is S_0. As the bubble grows the cell expands: $S^3 = S_0^3 + R^3$, where R is the bubble radius. The initial cell volume is determined by the number density, N_d, at nucleation:

$$\frac{4}{3}\pi S_0^3 = \frac{1}{N_d}. \quad (1)$$

The final bubble radius, R_f, is determined by the mass balance of volatiles:

$$R_f^3 \rho_{b,f} = S_0^3 \rho_m (C_s - C_f), \quad (2)$$

where $\rho_{b,f}$ and ρ_m are the final density of CO_2 in the bubble and melt density at equilibrium, C_s and C_f are initial and final concentration of CO_2 in the melt. The volatile concentration is pressure dependent and its difference $(C_s - C_f)$ is approximated for the limited

Table 2
Parameters used in the calculations

		Alkaline basalt	Kimberlite
Saturation pressure	P_0 (Pa)	$1.5 \cdot 10^9$ [a]	$5.0 \cdot 10^9$ [b]
Nucleation over-pressure	ΔP_n (Pa)	$2 \cdot 10^8$ [c]	
Temperature	T (°C)	1350 [c]	1350 [d]
Equation of state of CO_2	ρ_b (kg/m^3)	$743 + 3.6 \cdot 10^{-7} \cdot P_b$ [e]	$1500 + 10^{-7} \cdot P_b$ [e]
Solubility coefficient	K_S (Pa^{-1})	$1.3 \cdot 10^{-11}$ [a]	$10^{-10} - 2 \cdot 10^{-10}$ [f]
Melt density	ρ_m (kg/m^3)	2800 [g]	2800 [g]
Diffusivity	D (m^2/s)	10^{-10}–10^{-11} [h]	10^{-10}–10^{-11} [h]
Surface tension	σ (Pa m)	0.36 [i]	0.36 [i]
Compressibility	K_m (Pa)	$2 \cdot 10^{10}$ [g]	$2 \cdot 10^{10}$ [g]
Shear modulus	G (Pa)	$1.3 \cdot 10^{11}$ [j]	$1.3 \cdot 10^{11}$ [j]
Shear viscosity	η (Pa s)	<1 [k]	<1 [k]
Density dependence on CO_2 solubility	$\delta\rho_m/\delta C$ (kg/m^3)	3800 [g]	3800 [g]

[a] Holloway and Blank [35].
[b] Typical pressure derived from xenoliths in kimberlites.
[c] This study.
[d] Dalton and Presnall [36].
[e] Linear approximation, from: Saxena and Fei [37] for the relevant pressure range. P_b is fluid pressure in the bubble (Pa).
[f] Calculated based on Fig. 1 of Brey et al. [17], K_s varies with composition.
[g] Calculated based on density measurements of CO_2-bearing and CO_2-free alkaline basalt summarized in Fig. 3 of Lange [38]. We assumed the same density and compressibility for kimberlites.
[h] Diffusivity of CO_2 in mafic melts (Eqs. (26) (27) of Watson [39]).
[i] Murance and McBirney [40] and Walker and Mullins [41].
[j] Anderson [42].
[k] McKenzie [43]. Note that viscosity is only used for estimating the viscous relaxation time.

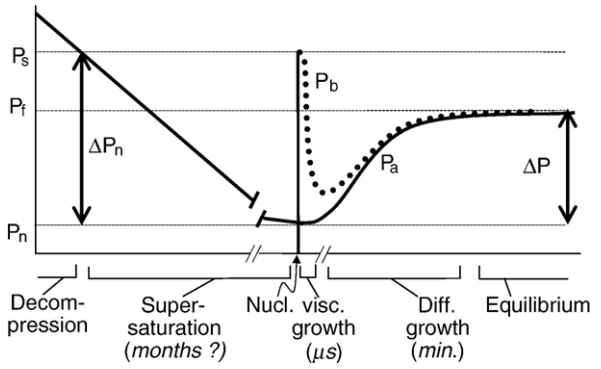

Fig. 4. Schematic diagram showing the temporal evolution of pressure. P_s is the saturation pressure, P_n is the nucleation pressure, $\Delta P_n = P_s - P_n$ is the supersaturation pressure, P_f is the final pressure and $\Delta P = P_f - P_n$ is the final overpressure. P_a is ambient pressure in the melt and P_b is the fluid pressure in the bubble, both vary with time. For example in the case of kimberlitic magma, P_s is 5.0 and P_n is 4.8 GPa. Note that the time scale along the x-axis varies; it is months during building of supersaturation, microseconds during nucleation and viscosity-controlled growth and minutes during diffusion-controlled stage and the approach to equilibrium.

pressure interval of nucleation [15] by a linear solubility law:

$$C_s - C_f = K_S(P_s - P_f), \tag{3}$$

where K_S is the pressure derivative of solubility at the relevant pressures. Gas density is also a function of pressure. For the narrow range of bubble pressures, P_b, relevant to the process of nucleation and growth of bubbles, the equation of state is approximately linear [28]:

$$\rho_b = A + B \cdot P_b. \tag{4}$$

The final bubble pressure, $P_{b,f}$, is balanced by the ambient pressure, P_f, and the surface tension at the bubble melt interface, σ:

$$P_{b,f} = P_f + 2\sigma / R_f. \tag{5}$$

The expansion of the bubbly magma deforms the surrounding host rock, which rebounds elastically. The stress distribution in the host rock around the expanding bubbly magma is approximated using stress distribution around a spherical inclusion in an infinite elastic medium [29]. Thus, the overpressure, $\Delta P = P_f - P_n$ (Fig. 4), is proportional to the volumetric deformation:

$$\Delta P = P_f - P_n = \frac{4}{3} G \frac{S_f^3 - S_0^3}{S_0^3}, \tag{6}$$

where G is the shear modulus of the host rock. The volumetric deformation of the bubbly magma, due to growth of the cell from S_0 to its final size S_f, may be represented as a sum of three different components:

$$\frac{S_f^3 - S_0^3}{S_0^3} = \frac{R_f^3}{S_0^3} - \frac{P_f - P_n}{K_m} + \frac{1}{\rho_m}\frac{\partial \rho_m}{\partial C}(C_s - C_f). \tag{7}$$

The first term on the right hand side is the strain due to the growth of bubbles to their final radius. This is the largest component contributing to the volume change. If the melt is compressible, two other terms should be added. One of them accounts for mechanical melt compaction due to pressure change (K_m is bulk modulus of the melt) and the second is due to the variation of density with volatile content. Substituting Eq. (7) into Eq. (6) and using Eqs. (2)–(4), yield the equation for the final over-pressure:

$$P_f - P_n = \frac{4}{3} G \left(\frac{K_S \rho_m}{A + B \cdot P_{b,f}} (P_s - P_f) - (P_f - P_n) \times \left(\frac{1}{K_m} + \frac{K_S}{\rho_m}\frac{\partial \rho_m}{\partial C} \right) \right). \tag{8}$$

Assuming that the final bubble radius is much larger than the radius at the nucleation, the surface tension in Eq. (5) may be neglected. Substituting $P_{b,f} = P_f$ into Eq. (8) provides an explicit relation for the final overpressure (see Appendix A), which depends only on melt properties (ρ_m, A, B, K_S, K_m, $\partial \rho_m / \partial C$) and rigidity ($G$) of the surrounding host rock (see Table 2). In this case, the final over pressure does not depend on the bubble number density (N_d). Numerical simulations show that even accounting for surface tension ($P_{b,f} > P_f$), the final pressure is almost insensitive to the number density of bubbles in the acceptable range ($N_d \sim 10^{10}$–10^{14} bubbles/m^3). Even at much higher number density ($N_d \sim 10^{16}$ bubbles/m^3) the reduction in $\Delta P / \Delta P_n$ due to the surface tension is less than 0.5%.

We calculate the overpressure that develops following nucleation in two magma types: alkaline basalts and kimberlites. This overpressure depends mostly on the pressure derivative of CO_2 solubility (K_S), which is about an order of magnitude greater in kimberlites than in alkaline basalts (Table 2). Fig. 5 presents the final overpressure (ΔP), normalized to supersaturation overpressure (ΔP_n) at various pressures and solubility coefficients. The effect of other parameters on the overpressure is minor.

The calculations show that the final stresses on the surrounding host rock reach ~30–45% of the supersaturation overpressure (ΔP_n). Adopting the experimental observation that a supersaturation pressure of ~200 MPa is needed to nucleate bubbles, the absolute

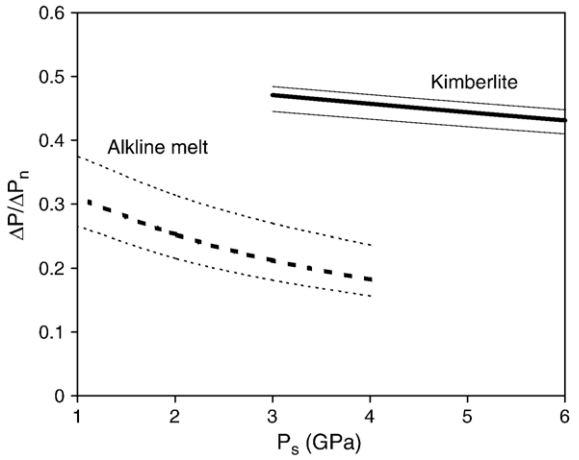

Fig. 5. Final gas overpressure (normalized to supersaturation) vs. saturation pressure (P_s) for kimberlitic and basic alkaline melts. In kimberlitic melt, about 45% of the supersaturation pressure may be recovered; in alkaline basic melts around 30%. The results are almost insensitive to the number density of bubbles but are sensitive to the choice of the solubility coefficient ($\partial C/\partial P$). For kimberlites, the solubility coefficient for the thick line is $1.5\cdot10^{-10}$ Pa^{-1} and the thin lines correspond to 10^{-10} (lower curve) and $2\cdot10^{-10}$ Pa^{-1} (upper curve). For alkaline melts the solubility coefficient is $1.3\cdot10^{-10}$ Pa^{-1} (with lower and upper values of 10^{-11} and $2\cdot10^{-11}$ Pa^{-1}, respectively). Curves were calculated using the data in Table 2.

value of final overpressure is as large as 90 MPa for kimberlites and 60 MPa for alkaline basalts. The minimal stress for tensional fracturing of mantle rocks is not well constrained, but is much lower than the above over-pressures [12]. The present data do not allow us to estimate the effect of heterogeneous nucleation on supersaturation. If the wall-rock minerals lower the critical supersaturation (similar to biotite in rhyolitic melt [25]), but do not obliterate it, then, the final overpressure may still be sufficient for fracturing. Still, to assure brittle failure of the surrounding rocks, pressure has to build up faster than ductile relaxation of the hot mantle rocks.

3.2. Time scale for pressure buildup

Growth is controlled by diffusion of volatiles into the bubbles. As noted above, the initial growth stage controlled by viscous deformation of the melt lasts only a few microseconds (Fig. 4), hence its duration is negligible in the present case. Later, growth is controlled by the diffusive flux of volatiles into the bubbles:

$$\frac{dm_b}{dt} = 4\pi R^2 D\rho_m \left.\frac{\partial C}{\partial r}\right|_R, \tag{9}$$

where D is the diffusivity of CO_2 and m_b is the mass of fluid in the bubble. The concentration gradient at the bubble-melt interface is approximated assuming quasi-static diffusion from an infinite shell [30]:

$$\left.\frac{\partial C}{\partial r}\right|_R = \frac{C_0 - C_R}{R}. \tag{10}$$

This approximation leads to recovery of 100% of the supersaturation pressure, and thus, to some over-estimation of the growth time. The equation for bubble growth rate is derived combining Eqs. (2), (3), (9) and (10), using the mass of volatiles in the bubble $m_b = \frac{4}{3}\pi R^3\rho_b$ (see Appendix B):

$$\frac{1}{R}\frac{dR}{dt} = \frac{D}{R^2}\frac{\rho_m}{A+BP_b}K_H(P_s - P_b). \tag{11}$$

This equation is coupled with the equations for bubble pressure and is solved numerically. However, it enables the time scale of bubble growth, $\tau = R/(dR/dt)$ to be defined. Substituting the final radius, solubility law, equation of state and the definition of number density (1)–(4) into Eq. (11) we obtain:

$$\begin{aligned}\tau &= \frac{R_f^2}{D}\frac{A+BP_{b,f}}{\rho_m}\frac{1}{K_H(P_n - P_{b,f})} \\ &= \left(\frac{9}{16\pi^2}\frac{A+BP_{b,f}}{\rho_m}\frac{1}{K_H(P_n - P_{b,f})}\right)^{\frac{1}{3}}\frac{1}{DN_d^{2/3}}.\end{aligned} \tag{12}$$

Eq. (12) defines the upper limit of the growth time scale, since we assume an infinite shell in Eq. (10), and use the final bubble radius. The time scale for pressure buildup depends mostly on bubble number density and CO_2 diffusivity and weakly on other melt properties. *The resulting time scale ranges from seconds up to a day* for an extreme range of number densities and for the possible range of CO_2 diffusivity (Fig. 6).

3.3. Comparison of time scales for loading and relaxation

The time scale for pressure buildup compared with the characteristic time scales for stress relaxation allows an evaluation of the potential for brittle fragmentation. Two mechanisms for stress relaxation are accounted in this discussion. One relaxation mechanism is by viscous deformation of the surrounding rocks, and the second is by the viscous flow of the melt from the nucleation region back towards the source region.

The stress relaxation by viscous deformation of the surrounding rocks is characterized by the Maxwell time, the ratio between the viscosity and shear modulus of the mantle $\tau_{Maxwell} = \eta_{mantle}/G_{mantle}$. The lower bound estimation of the Maxwell time is obtained using

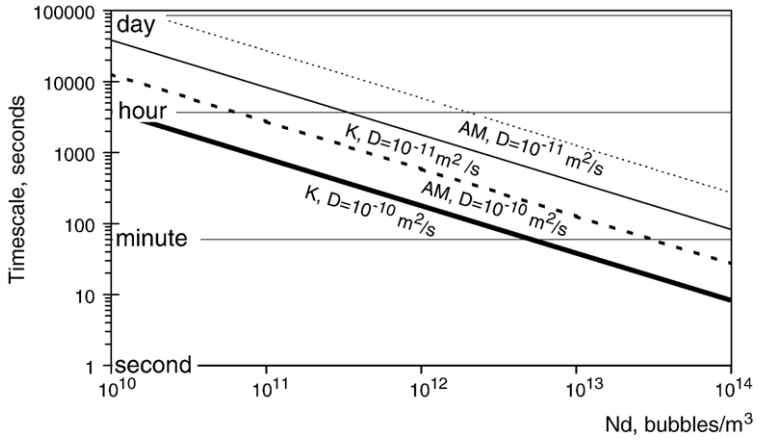

Fig. 6. Time scale of pressurization vs. number density. Solid lines stand for kimberlitic melt and dashed lines for alkaline basic melts; thick lines for diffusivity of 10^{-10} m^2/s and thin lines 10^{-11} m^2/s. For the typical case (lab and natural samples) $N_d \sim 10^{12}$ bubbles/m^3, which means that pressurization time scale is less than an hour.

astenospheric values: mantle viscosity, $\eta_{mantle} > 10^{19}$ Pa s and rigidity, $G_{mantle} \sim 10^{11}$ Pa [31]. Even under these conditions, the Maxwell time is years or longer. The ratio between the Maxwell time scale and the pressurization time scale is above 10^2 for extremely low number density, and of the order of 10^4 for the more realistic number density ($N_d \sim 10^{12}$ bubbles/m^3). The above estimates show that following nucleation and bubble growth, overpressure is large and pressurization is fast enough to fracture the surrounding rocks, if the magma is confined.

We now consider whether the flow of magma back into the "tail" it leaves behind during ascent may relax the excess pressure that is built up following a nucleation event. The existence of such tails is suggested by experiments with analog materials (e.g., [32,33]). The 200 MPa of supersaturation means that the distance between the saturation and the nucleation level is about 10 km, suggesting a high aspect ratio so that even if the nucleation region is connected to the source region, the channel is expected to be very narrow. Heimpel and Olson [32] suggested an experimentally based scaling for the rate of ascent of a buoyant viscous drop through a visco-elastic medium. They estimated the thickness of the tail to be of the order of a millimeter for mantle conditions. Even thinner tails (magmatic channels in the mantle) are discussed by Ito and Martel [33] using a scaling analysis based on the formulation of Rubin [34]. We estimate the characteristic time of pressure relaxation by a Poiseuille flow driven by a pressure difference of 50 MPa between the nucleation and saturation depth (a few kilometers). For a channel of 1 mm width filled with low viscosity magma (~10 Pa s), relaxation takes over a month.

The analysis presented above shows that *the time scales of the two relaxation processes are much longer than the pressurization time scale (seconds to a day). Thus we conclude that pressure builds up fast enough to fragment the surrounding host rocks*.

4. Implications for xenolith entrapment and dike initiation

The mechanism suggested here implies a discrete event of crack formation. Such an event involves breaking of the host rocks at the site of nucleation and should lead to entrapment of xenoliths in the ascending magma. That means that many of the xenoliths carried by the erupting magma originate from a limited depth range. Although we did not find any specific reference in the literature for similar depth of origin for xenoliths in a specific eruption, it is our experience that on many occasions, alkaline basalts do carry nodules from either the mantle or the lower crust, and that sampling of both depth ranges in a single flow is rare. We suggest that nucleation leads to "explosion" and that such "explosions" fracture the wall rocks and form the xenoliths. The depth of such events is controlled by the original volatile content of the magma. Of course, more xenoliths may be trapped at later stages due to branching of the dike and the creation of a process zone around it.

When the surrounding mantle rocks fracture, magma penetrates into the newly formed cracks and widens them. More important, the exsolving low viscosity CO_2-rich fluid may now penetrate into the crack and increase the stress at the tip. Such a pressure-driven crack accelerates and may evolve into a new dike. Fluid flow

into the tip is expected to continue as the bubbly magma ascends and fills the propagating dike. Thus, continued exsolution of the decompressed magma may enhance the role of pressure-driven propagation mechanism and ensure fast ascent. A similar transition from a buoyancy to a pressure driven mechanism of dike ascent near the saturation depth was previously discussed by Rubin [14].

5. Summary

We studied the nucleation of CO_2 bubbles in mafic alkaline magma. Samples were saturated at 1.5 GPa, 1350 °C, decompressed by 0–1 GPa, and quenched after 5–40 min at the lower pressure. No bubbles were found after decompression by 100 MPa and in one experiment even when decompression was 300 MPa. Up to $2.5{\cdot}10^{15}$ bubbles/m^3 were observed when pressure was dropped by 300 MPa or more. We conclude that the critical supersaturation pressure is 200±100 MPa.

Melts formed by small degrees of partial melting are rich in volatiles and may reach the above critical level of supersaturation by slow ascent or by partial crystallization. Following nucleation, the excess CO_2 in the melt diffuses into the bubbles. If magma volume is confined, bubble growth leads to deformation of the surrounding walls and pressure increases towards mechanical and chemical equilibrium. Modeling the growth, and accounting for melt and walls compressibility, we found that about 30% of the supersaturation pressure can be recovered in alkaline basalts. Kimberlites, with stronger dependence of solubility on pressure may recover about 45% of the supersaturation pressure. The time scale for growth and pressurization is of the order of seconds to days, much shorter than the Maxwell relaxation time of the walls, or the characteristic time for flow back towards the source.

We conclude that nucleation and growth of CO_2 bubbles in supersaturated magmas may build up pressures of tens of MPa, more than enough to initiate cracks in the surrounding wall rocks. Such a cracking event can form xenoliths and initiate dikes that allow the transport of the magma and its xenoliths to the surface. This mechanism may explain the limited depth range from which many of the xenoliths sampled by individual eruptions originate, as is often observed.

Acknowledgements

Research was funded by the Israel–US Binational Science Foundation. The bubble nucleation research was supported by NSF EAR 9506494 and EAR-0208456 to JRH. ON and VL acknowledge partial support from the MULTIMO (EVGI-CT-2000-0021) supported by the Environmental and Sustainable Development Program of the European Commission Research Directorate General.

Appendix A. Numerical procedure to solve P_f and R_f

To calculate the final radius and pressure, we have to solve Eq. (8). Neglecting the surface tension at the final stage, when the bubbles are much larger than the critical radius at nucleation ($P_f = P_{b,f}$), Eq. (8) is:

$$P_f - P_n = \frac{4}{3} G \left(\frac{K_H \rho_m}{A + B \cdot P_f} (P_s - P_f) - (P_f - P_n) \times \left(\frac{1}{K_m} + \frac{K_H}{\rho_m} \frac{\partial \rho_m}{\partial C} \right) \right). \quad \text{(A1)}$$

This is a quadratic equation for P_f:

$$a P_f^2 + b P_f + c = 0, \quad \text{(A2)}$$

with the coefficients of the polynom:

$$\begin{aligned} a &= B \left[1 + \frac{4}{3} G \left(\frac{1}{K_m} + \frac{K_H}{\rho_m} \frac{\partial \rho_m}{\partial C} \right) \right] \\ b &= \frac{4}{3} G K_H \rho_m + \left(1 + \frac{4}{3} G \right) \left(\frac{1}{K_m} + \frac{K_H}{\rho_m} \frac{\partial \rho_m}{\partial C} \right) (A - B P_n) \\ c &= A P_n - \frac{4}{3} G K_H \rho_m P_s - \frac{4}{3} G A P_n \left(\frac{1}{K_m} + \frac{K_H}{\rho_m} \frac{\partial \rho_m}{\partial C} \right), \end{aligned} \quad \text{(A3)}$$

which has positive and negative solutions. The positive solution for P_f is:

$$P_f = \frac{-b + \sqrt{b^2 - 4ac}}{2a}. \quad \text{(A4)}$$

This solution can be corrected for the surface tension using the iteration procedure that starts with calculation of the final radius:

$$R_f^3 = S_0^3 \rho_m K_H \frac{P_s - P_{b,f}}{A + B P_{b,f}}. \quad \text{(A5)}$$

This equation is derived by substituting Eqs. (2) and (3) into Eq. (1). The calculated R_f is substituted into Eq. (5) to obtain the corrected $P_{b,f}$ for the surface tension and then Eq. (A1) is solved for P_f, using the $P_{b,f}$ obtained at the previous step. This iteration procedure is repeated until the solution converges.

Appendix B. Equation for bubble growth

The time derivative of the mass of volatiles inside the bubble, $m_b = \frac{4}{3}\pi R^3 \rho_b$, is:

$$\frac{dm_b}{dt} = \frac{4}{3}\pi\left(\frac{dR^3}{dt}\rho_b + R^3\frac{d\rho_b}{dt}\right). \quad (B1)$$

Substituting Eq. (B1) into Eq. (9) yields:

$$\frac{4}{3}\pi\left(\frac{dR^3}{dt}\rho_b + R^3\frac{d\rho_b}{dt}\right) = 4\pi R^2 D\rho_m \left.\frac{\partial C}{\partial r}\right|_R. \quad (B2)$$

Then substituting Eq. (10) into Eq. (B2) yields:

$$\frac{3}{R}\frac{dR}{dt} + \frac{1}{\rho_g}\frac{d\rho_g}{dt} = 3\frac{D}{R^2}\frac{\rho_m}{\rho_g}(C_0 - C_R). \quad (B3)$$

Eq. (B3), which describes the kinetics of bubble growth, may be simplified if one of the terms on the left hand side is much smaller than the other. The ratio between the first and second terms is:

$$3\frac{\delta R}{R}\Big/\frac{\delta\rho_b}{\rho_b}. \quad (B4)$$

The first term is very large since the system contains small nuclei bubbles which grow significantly $\delta R/R \gg 1$. The second term is very small since the pressure drop is much smaller than the lithostatic pressure in the nucleation region $\delta\rho_g/\rho_g \ll 1$. Thus the ratio (B4) is very large, meaning that the second term in Eq. (B3) is negligible and Eq. (B3) simplifies to:

$$\frac{1}{R}\frac{dR}{dt} = \frac{D}{R^2}\frac{\rho_m}{\rho_g}(C_0 - C_R). \quad (B5)$$

Substituting the solubility law (2) and the equation of state (3) we obtain the equation for bubble growth (11).

References

[1] D.H. Eggler, Kimberlites: how do they form? in: J. Ross, et al., (Eds.), Kimberlites and Related Rocks, Blackwell, Melbourne, 1989, pp. 489–504.

[2] G.P. Brey, T. Kohler, Geothermometry in four-phase lherzolites II. New thermobarometers, and practical assessment of existing thermobarometers, J. Petrol. 31 (1990) 1353–1378.

[3] V. Sautter, S.E. Haggerty, S. Field, Ultra deep (>300 km) ultramafic xenolites: new petrologic evidence from the transition zone, Science 252 (1991) 827–830.

[4] A.E. Ringwood, S.E. Kesson, W. Hibberson, N. Ware, Origin of kimberlites and related magmas, Earth Planet. Sci. Lett. 113 (1992) 521–538.

[5] K.D. Collerson, S. Hapugoda, B.S. Kamber, Q. Williams, Rock from the mantle transition zone: majorite-bearing xenoliths from Malaita, Southern Pacific, Science 288 (2000) 1215–1223.

[6] D. Canil, Y. Fedortchouk, Garnet dissolution and the emplacement of kimberlites, Earth Planet. Sci. Lett. 167 (1999) 227–237.

[7] S.P. Kelley, J.-A. Wartho, Rapid kimberlite ascent and the significance of Ar–Ar ages in xenolith phlogopites, Science 289 (2000) 609–611.

[8] F.J. Spera, Carbon dioxide in petrogenesis III: role of volatiles in the ascent of alkaline magma with special reference to xenolith-bearing mafic laves, Contrib. Mineral. Petrol. 88 (1984) 217–232.

[9] V.A. Milashev, Explosion Pipes, Springer-Verlag, New York, 1988. 249 pp.

[10] J. Phipps Morgan, T.J. Reston, C.R. Ranero, Contemporaneous mass extinctions, continental flood basalts, and 'impact signals': are mantle plume-induced lithospheric gas explosions the causal link? Earth Planet. Sci. Lett. 217 (2004) 263–284.

[11] D.A. Spence, D.L. Turcotte, Bouyancy-driven magma fracture; a mechanism for ascent through the lithosphere and the emplacement of diamonds, J. Geophys. Res. 95 (1990) 5,133–5,139.

[12] A.M. Rubin, Dikes vs. diapirs in viscoelastic rock, Earth Planet. Sci. Lett. 119 (1993) 641–659.

[13] A.M. Rubin, D. Gillard, Dike-induced earthquakes: theoretical considerations, J. Geophys. Res. 103 (1998) 10017–10030.

[14] A.M. Rubin, Propagation of magma-filled cracks, Annu. Rev. Earth Planet. Sci. 23 (1995) 287–336.

[15] J.R. Holloway, J.G. Blank, Application of experimental results to C–O–H species in natural melts, in: J.R. Holloway (Ed.), Volatiles in Magmas, Mineralogical Society of America, Washington, D.C., 1994, pp. 187–230.

[16] J.E. Dixon, D.A. Clauge, P. Wallace, R. Poreda, Volatiles in alkali basalts from the North Arch Volcanic Field, Hawaii: extensive degassing of deep submarine-erupted alkalic series lavas, J. Petrol. 38 (1997) 911–939.

[17] G.P. Brey, L.N. Kogarko, I.D. Ryabchikov, Carbon dioxide in kimberlitic melts, Neues Jahrb. Mineral., Monatsh. 4 (1991) 159–168.

[18] H.R. Shaw, Viscosities and magmatic silicate liquids: an empirical method of prediction, Am. J. Sci. 272 (1972) 870–893.

[19] V. Pan, J.R. Holloway, R.L. Hervig, The pressure and temperature dependence of carbon dioxide solubility in tholeiitic basalt melts, Geochim. Cosmochim. Acta 55 (1991) 1587–1595.

[20] S. Esperanca, J.R. Holloway, The origin of the high-K latites from Camp Creek, Arizona: constraints from experiments with variable fO_2 and aH_2O, Contrib. Mineral. Petrol. 93 (1986) 504–512.

[21] Y. Thibault, J.R. Holloway, Solubility of CO_2 in a Ca-rich leucitite: effects of pressure, temperature and oxygen fugacity, Contrib. Mineral. Petrol. 116 (1994) 216–224.

[22] M. Mangan, T. Sisson, Delayed disequilibrium degassing in rhyolite magma: decompression experiments and implications for explosive volcanism, Earth Planet. Sci. Lett. 183 (2000) 441–455.

[23] C.C. Mourtada-Bonnefoi, D. Laporte, Homogeneous bubble nucleation in rhyolitic magmas: an experimental study of the effect of H_2O and CO_2, J. Geophys. Res. Sol. 107 (2002) 2066.

[24] M. Mangan, T. Sisson, Evolution of melt-vapor surface tension in silicic volcanic systems: experiments with hydrous melts, J. Geophys. Res. 110 (2005) B01202, doi:10.1029/2004JB003215.

[25] S. Hurwitz, O. Navon, Bubble nucleation in rhyolitic melts: experiments at high pressure, temperature and water content, Earth Planet. Sci. Lett. 122 (1994) 267–280.

[26] A.V. Girnis, G.P. Brey, I.D. Ryabchikov, Origin of group 1A kimberlites: fluid-saturated melting experiments at 45–55 kbar, Earth Planet. Sci. Lett. 134 (1995) 283–296.

[27] O. Navon, V. Lyakhovsky, Vesiculation processes in silicic magmas, in: R.S.J. Sparks (Ed.), The Physics of Explosive Volcanic Eruptions, The Geological Society of London, London, 1998, pp. 27–50.
[28] D.J. Frost, B.J. Wood, Experimental measurements of the properties of H_2O–CO_2 mixtures at high pressures and temperatures, Geochim. Cosmochim. Acta 61 (1997) 3301–3309.
[29] T.M. Atanackovic, A. Guran, Theory of Elasticity for Scientists and Engineers, Birkhauser Verlag, Basel, 2000. 374 pp.
[30] V. Lyakhovsky, S. Hurwitz, O. Navon, Bubble growth in rhyolitic melts: experimental and numerical investigation, Bull. Volcanol. 58 (1996) 19–32.
[31] D.L. Turcotte, G. Schubert, Geodynamics Applications of Continuum Physics to Geological Problem, John Wiliey & Sons, New York, 1982. 450 pp.
[32] M. Heimpel, P. Olson, Buoyancy-driven fracture and magma transport through the lithosphere: models and experiments, in: M. P. Ryan (Ed.), Magmatic Systems, Academic Press, San Diego, Calif., 1994, pp. 223–240.
[33] G. Ito, S.J. Martel, Focusing of magma in the upper mantle through dike interaction, J. Geophys. Res. 107 (B10) (2002) 2223, doi:10.1029/2001JB000251.
[34] A.M. Rubin, Dike ascent in partially molten rock, J. Geophys. Res. 103 (1998) 20,901–20,919.
[35] L.H. Slordal, E.A. Martinsen, A.F. Blumberg, Modeling the Response of an Idealized Coastal Ocean to a Traveling Storm and to Flow Over Bottom Topography, 1994.
[36] J.A. Dalton, D.C. Presnall, The continuum of primary carbonatitic–kimberlitic melt compositions in equilibrium with lherzolite; data from the system CaO–MgO–Al_2O_3–SiO_2–CO_2 at 6 GPa, J. Petrol. 39 (1998) 1953–1964.
[37] S.K. Saxena, Y. Fei, High pressure and high temperature fluid fugacities, Geochim. Cosmochim. Acta 51 (1987) 783–791.
[38] R.A. Lange, The effect of H_2O, CO_2 and F on the density and viscosity of silicate melts, in: J.R. Holloway (Ed.), Volatiles in Magmas, Mineralogical Society of America, Washington, D.C., 1994, pp. 331–365.
[39] E.B. Watson, Diffusion in volatile-bearing magmas, in: J.R. Holloway (Ed.), Volatiles in Magmas, Mineralogical Society of America, Washington, D.C., 1994, pp. 371–409.
[40] T. Murace, A. McBirney, Properties of some common igneous rocks and their melts at high temperatures, Geol. Soc. Amer. Bull. 84 (1973) 3536–3592.
[41] D. Walker, O.J. Mullins, Surface tension of natural silicate melts from 1200 degrees–1500 degrees C and implications for melt structure, Contrib. Mineral. Petrol. 76 (1981) 455–462.
[42] D.L. Anderson, Theory of Earth, Blackwell Scientific Publications, Oxford, 1989. 355 pp.
[43] D. McKenzie, The extraction of magma from the crust and mantle, Earth Planet. Sci. Lett. 74 (1984) 81–91.